Article:
Munive Olarte, A. orcid.org/0000-0002-8612-5001, Durgut, E. orcid.org/0000-0002-2224-7325, Verbruggen, S. orcid.org/0000-0002-2321-1367 et al. (2 more authors) (2025) Particle stabilised high internal phase emulsion scaffolds with interconnected porosity facilitate cell migration. Biomedical Materials. ISSN: 1748-6041

https://doi.org/10.1088/1748-605x/ae05de

Biomedical Materials

PURPOSE-LED PUBLISHING™

Particle stabilised high internal phase emulsion scaffolds with interconnected porosity facilitate cell migration

To cite this article before publication: Areli Munive Olarte *et al* 2025 *Biomed. Mater.* in press https://doi.org/10.1088/1748-605X/ae05de

IOP PublishingJournal Title
Journal **XX** (XXXX) XXXXXX https://doi.org/XXXX/XXXX

Particle stabilised high internal phase emulsion scaffolds with interconnected porosity facilitate cell migration

Areli Munive-Olarte[1,2], Enes Durgut[3], Stefaan W. Verbruggen[4], Frederik Claeyssens [1,2] and Gwendolen C. Reilly [1,2]

[1] Kroto Research Institute, School of Chemical, Materials and Biological Engineering, University of Sheffield, United Kingdom.

[2] INSIGNEO Institute for in Silico Medicine, School of Chemical, Materials and Biological Engineering, University of Sheffield, United Kingdom.

[3] Department of Genetics and Bioengineering, Alanya Alaaddin Keykubat University, Alanya, Turkiye.

[4] Centre for Predictive in-vitro models and Centre for Bioengineering, School of Engineering and Materials Science, Queen Mary University of London, United Kingdom.

Email:
g.reilly@sheffield.ac.uk

Abstract

A key challenge in bone tissue engineering (BTE) is designing structurally supportive scaffolds, mimicking the native bone matrix, yet also highly porous to allow nutrient diffusion, cell infiltration, and proliferation. This study investigated the effect of scaffold interconnectivity on human bone marrow stromal cell (BMSC) behaviour. Highly interconnected, porous scaffolds (polyHIPEs) were fabricated using the emulsion templating method from 2-ethylhexyl acrylate/isobornyl acrylate (IBOA) and stabilised with ~200 nm IBOA particles. Pore interconnectivity was tuned by varying the internal phase fraction from 75 to 85% and characterised by the degree of openness (DOO), Euler number, frequency and size of pore interconnects. The attachment, proliferation, infiltration, and osteogenic differentiation of the BMSC cell line (Y201) were evaluated on these scaffolds. Results showed that high pore interconnectivity facilitated diffusion and cell infiltration throughout the scaffolds. Furthermore, the most interconnected scaffolds enhanced osteogenic differentiation of Y201 cells, as evidenced by elevated alkaline phosphatase (ALP) activity and increased calcium and collagen production compared to less interconnected scaffolds. These findings emphasise the importance of scaffold interconnectivity in BTE for efficient nutrient transport, facilitating cell migration and infiltration, and supporting the development of interconnected cell networks that positively influence osteogenic differentiation.

Keywords: Bone scaffold, pore interconnectivity, cell infiltration, osteogenic differentiation, tissue engineering.

1. Introduction

Bone Tissue Engineering (BTE) seeks to promote bone regeneration by combining biomaterials, bone progenitor cells, and growth factors synergistically. Biomaterials serve as scaffolds to support cell proliferation and bone extracellular matrix formation. Whether used as bone graft substitutes or *in-vitro* models, scaffolds require a three-dimensional (3D) porous architecture that facilitates cell infiltration and effective nutrient solute transport (1).

Characteristics like pore size, porosity, and pore interconnectivity are structural features that affect cell mechanobiology, influencing cell attachment, growth, cell migration, vascularization, and nutrient-waste exchange (2,3) There is no consensus about the optimal pore size for scaffolds in BTE, but small pores can reduce cell migration and fluid flow, while large pores may reduce the available surface area, limiting cell attachment (2,4) Moreover, mesenchymal stem cells (MSC) in confined areas with low contractibility favour an adipogenic fate, whereas larger spaces are more likely to support an osteogenic lineage (5). A high porosity in scaffolds is desired because of the higher surface area, providing more space for cells to attach, migrate, grow, and interact. *In-vitro* studies using scaffolds with 70% or greater porosity supported better bone ingrowth and osteogenic differentiation (6). Generally, high porosity correlates with high permeability within a scaffold. However, scaffolds with similar pore size and porosity can have different permeabilities (7). This is because, a high porosity alone does not always describe how accessible and interconnected the pores are. A more comprehensive assessment of scaffold openness includes factors such as permeability, porosity, pore size, pore interconnectivity, and the dimensions and distribution of pore interconnects (8). Some of the methods for calculating these parameters on scaffolds include scanning electron microscopy (SEM) (9), mercury intrusion porosimeter (10), x-ray microcomputed tomography (11), nano-computed tomography (12), permeability measurements (13) permeability simulations (14) or pore volume/surface area measurements (10).

Among the techniques used to produce more open or interconnected scaffolds are 3D printing (15), salt leaching (16) gas foaming (17) freeze-drying (18), porogens (19), and emulsion templated scaffolds (12). The emulsion templating method enables the production of polymerised emulsions with high internal phase volumes (≥74%) (HIPEs). The empty spaces generated by HIPEs polymerisation to form polyHIPEs and subsequent water removal are called pores or voids, and the narrow passages that connect those are called pore throats, windows, or interconnects (20).

PolyHIPEs can be fabricated in various shapes using casting techniques, stereolithography, 3D printing, or electrospinning (9). As emulsions consist of two immiscible liquids, a surfactant or particles are needed to stabilise them. While surfactants reduce the oil-water interfacial tension, particles create a mechanical barrier between the phases. Particle-stabilised polyHIPEs, known as pickering polyHIPEs, or polyHIPPEs, offer advantages over surfactant-stabilised ones, including enhanced mechanical properties, permeability, and larger pores (20). However, pickering polyHIPEs are typically associated with closed pores due to the thick interfacial barrier between the emulsion phases. In a recent study, acrylate particles were used to stabilise HIPEs via arrested coalescence (10). This mechanism enabled the production of larger pore polyHIPEs with interconnected porosity. Additionally, a tuneable pore size and interconnectivity was achieved by adjusting the volume of the internal phase and the size and concentration of particles. While pore size and porosity of scaffolds have been often compared for their effects on MSC responses, pore interconnectivity has received less attention. Therefore, this study aims to investigate the effect of pore interconnectivity within pickering polyHIPEs on the behaviour of MSCs, focusing on the infiltration and migration into the scaffolds.

2. Materials and Methods

2.1 Isobornyl acrylate particle preparation

IBOA particles were used to stabilise the HIPEs. Particles around 200 nm were fabricated via the ultrasound-assisted oil-in-water (o/w) emulsion polymerisation method (Figure 1) (10). In brief, per 9 g of the continuous phase, 1 g of the internal phase is used. Both are mixed for 2 min using a sonicator at 100 W, 30 kHz (Hielscher UP100H, Hielscher Ultrasound Technology). The continuous phase consisted of 0.5 wt.% of Tween 20 (P2287, Sigma Aldrich) in deionised water (dH_2O), while the internal phase was a blend of 75 wt.% IBOA (392103, Sigma)/ 25 wt.% trimethylolpropane triacrylate (TMPTA) (246808, Merck) and 2 wt.% potassium persulfate (216224, 99%,

Sigma) as the initiator. The emulsion was polymerised in a convection oven at 65 °C for 18 h. Particles were washed with methanol (99.9 %, Fisher, UK) under agitation for 15 min and centrifuged at 4000 rpm for 10 min. Then, the supernatant was replaced with 10 mL of dH_2O and dispersed with a sonicator at 100 W, 30 kHz, for 1 min. Finally, the particles were dried overnight in an oven at 65 °C.

2.2 Fabrication of polyHIPEs

HIPEs were prepared by mixing a 2-ethylhexyl acrylate (EHA) (290815, 98%, Sigma)/IBOA blend with the respective amount of dH_2O for a 75, 80, or 85 (% v/v) internal phase (10). In detail, the blend was prepared by mixing 63 wt.% EHA, 21 wt.% IBOA, 16 wt.% TMPTA, and 5 wt.% IBOA particles by sonication (100 W, 30 kHz) for 1 min. The corresponding volume of dH_2O was added to the monomer phase at a constant flow rate of 0.8 mL min^{-1} using a syringe pump (18 mm), while the monomer blend was under agitation using an overhead stirrer (Pro40, SciQuip) at 500 rpm. Subsequently, the photo-initiator 0.1 g of 2-hydroxy-2-methylpropiophenone (405655, 95%, Sigma) per 4 g of monomer blend was added. Emulsions were photopolymerised using a belt conveyor ultraviolet curing system (GEW Engineering UV) and dried in an oven at 60 °C for 18 h. Then, polyHIPEs were washed with methanol to remove the uncured monomers. Samples were named according to the %v/v of the internal phase preceding a H for HIPEs and a P for polyHIPEs. For instance, P75 was a polyHIPE with an internal phase of 75% v/v. All reagents and equipment were kept constant across all groups (P75, P80, P85). Samples from each experimental group were assigned using the lottery method for polyHIPEs characterisation.

2.3 PolyHIPEs characterisation

PolyHIPE samples were prepared for SEM imaging by first removing outer layers with a scalpel. Cuboid cross-sections (1 x1 x 0.5 mm, n = 3 per group) were then cut from these inner regions. Each cross-section was gold-coated and imaged using a SEM (Inspect F, FEI), operated with an acceleration voltage of 15 kV and a spot size of 3.5 in secondary electron mode. Image J (https://imagej.net/ij/download.html) was used to measure the diameter of pores (n = 300), diameter of pore interconnects, also known as pore throats or windows (n = 200), and number of pore interconnects per pore (n =50) from SEM micrographs. For the diameter, around 40 random pores/interconnects were measured from six SEM micrographs for each polyHIPE. A statistical correction factor (2√3) was applied, considering the uneven sectioning of the sample (9,10).

DOO is the ratio of the open surface to the total surface of a pore. It was determined in polyHIPEs (n = 20) according to equation (1), where A*w* is the surface area of the interconnects and Aρ is the surface area of the pore (10). The pore surface was considered the curved surface area of a hemisphere. ImageJ was used to adjust the threshold to improve pore/interconnects identification and measured using the analyse particles plugin or by measuring the diameters of pores or interconnects.

$$DOO = \frac{\sum Aw}{A_P} \quad (1)$$

The porosity and apparent density (ρ) of the polyHIPEs (n = 3 per group) were measured by the ethanol displacement method, equations (2, 3). Dry samples were weighed (W0) and placed in a known volume of ethanol (99.8 %, Fisher) (V1) for 5 min, then vacuumed to evacuate the air and allow the ethanol to enter the pores of the scaffold. The total volume of the ethanol impregnated in the scaffold (V2), the weight of the wet scaffolds (W1), and the remaining ethanol (V3) were recorded (21).

$$Porosity\ (\%) = \frac{V1-V3}{V2-V3} * 100 \quad (2)$$

$$\rho = \frac{W0}{V2-V3} \quad (3)$$

PolyHIPEs were scanned dry using a SkyScan 1272 3D X-ray microscope (Bruker). Imaging parameters included pixel size of 4.0 µm, a source voltage of 50 kV, and a source current of 200 µA. Before analysis, the dataset was processed with thresholding, filtering, and despeckle tools using CTAn software (Brucker) to reduce the noise. Euler number was calculated, and 3D visualisation were generated with CTvox software (Brucker).

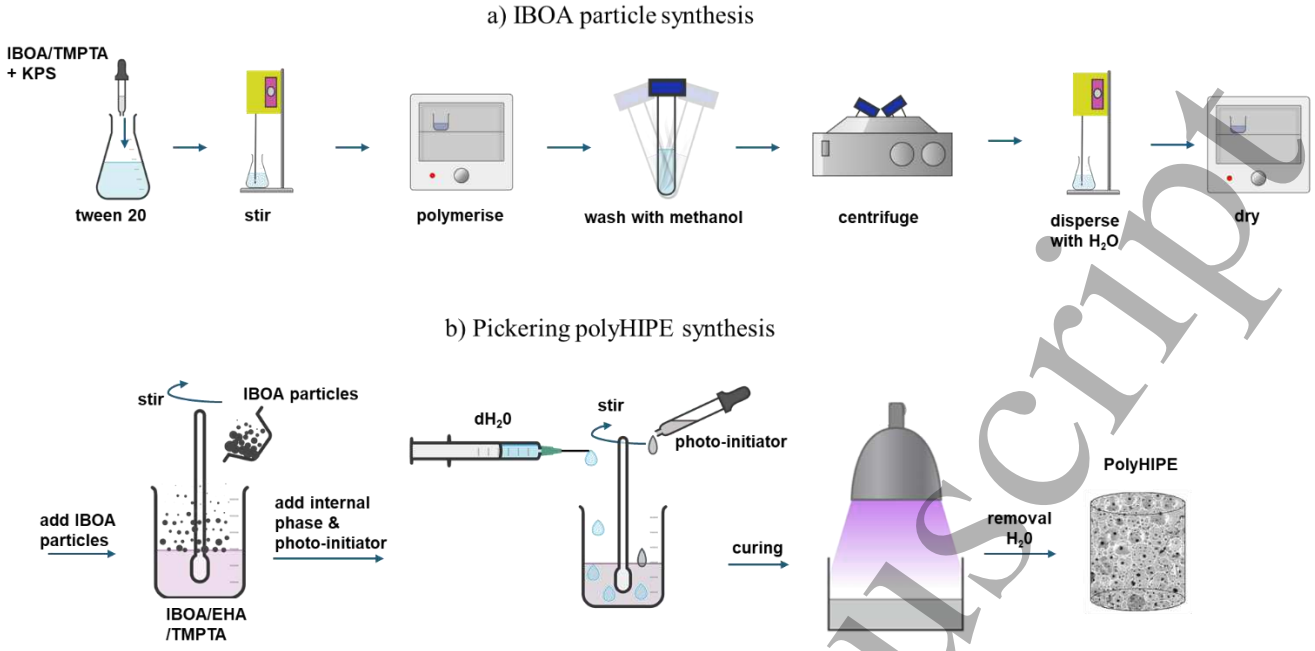

Figure 1: Schematic representation for the preparation of IBOA particles and pickering polyHIPEs, created with Chemix (2025), from https://chemix.org.

2.4 Dextran diffusion

PolyHIPEs were cut into 4 mm diameter and 2 mm height using a cork borer. Then their sides were cut off using a scalpel to eliminate any non-porous external layer. Samples were treated in a vacuum plasma cleaner (Zepto, Diener Electronic) at 0.8 mbar with a power of 50W for 60 s to increase their hydrophilicity (22). These were stained with 0.3 wt.% Sudan black B (199664, Sigma) in 70% ethanol, and excess was removed with three washes of phosphate-buffered saline (PBS) (P4417, 1X, Sigma-Aldrich). PolyHIPEs (n = 3 per group) were glued (ethyl-2-cyanoacrylate, UHU GmbH & Co.) to petri plates and hydrated with dH_2O for 4 h. dH_2O was removed, and a solution of 0.1 mg mL^{-1} fluorescein isothiocyanate-dextran (FITC-dextran) (FD150, 150 kDa, Sigma) prepared in PBS was poured into the petri dish until the height of the scaffold (23). After 15 min, imaging was performed on a confocal fluorescent microscope (Leica SP8 TCS Microscope, UK) at room temperature (RT) using a 488 nm laser and 10X objective. The relative fluorescence intensity was measured using ImageJ software.

2.5 Cell Culture

A human telomerase reverse transcriptase immortalised (hTERT) BMSC clonal line Y201 (CVCL_VG68) was used in all experiments. The Y201 line was selected because it maintained a mesenchymal morphology and tripotent differentiation (adipogenic, chondrogenic, and osteogenic) when induced chemically (24). This clone line was donated from Professor Paul Genever (University of York) under a material transfer agreement (MTA). Y201 BMSCs were maintained in basal medium consisting of Dulbecco's Modified Eagle Medium (42430025, LOT# 2605210, Gibco), supplemented with 10% v/v foetal bovine serum (FBS) (A5256701, LOT# 08Q5283K, Gibco) and 1% v/v (100 I.U mL^{-1}—100 µg mL^{-1}) penicillin-streptomycin (P4333, LOT# 0000137186, Sigma) (25). Cells were maintained in a humidified incubator at 37 ºC and 5% CO_2. Cultures were passaged at 80% confluence using Trypsin-EDTA (T4049, LOT# SLCL2418, Sigma) and frozen down with a cryo-freezing container at -80 ºC in 10% v/v dimethyl sulfoxide (D2650, LOT# RNBK3096, Sigma) in FBS for 24 h and later stored in liquid nitrogen until use. A mycoplasma analysis was performed before cell seeding using a mycoplasma detection kit (rep-mysnc-50, InvivoGen).

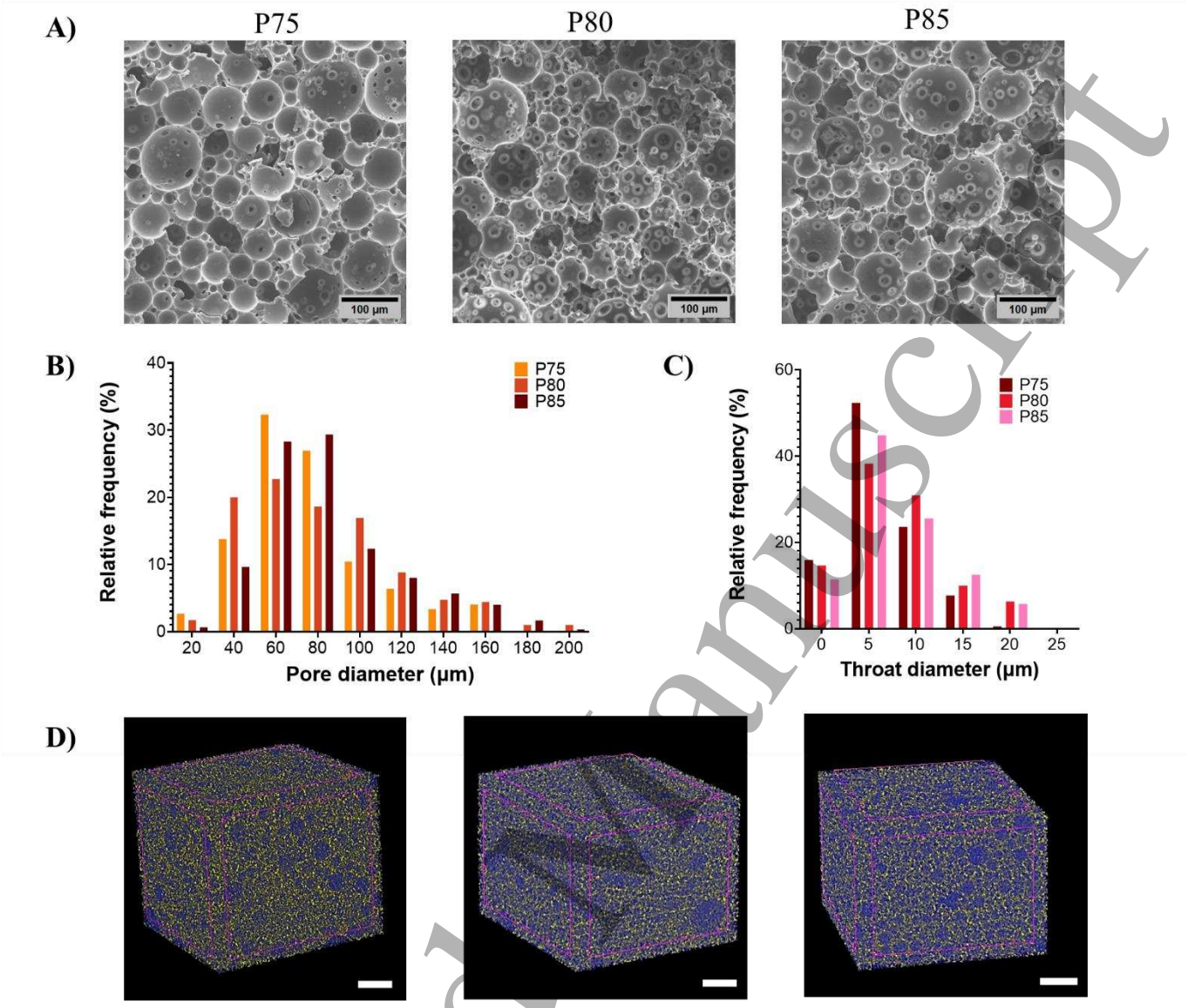

Figure 2. SEM images and pore size analysis of scaffolds. A) SEM images of cross-sections of polyHIPEs with internal phases of 75, 80, and 85 (% v/v) stabilised by IBOA nanoparticles. B) Histogram of pore diameter distribution (n = 300), and C) pore throat size (n = 200) measured from SEM images. D) 3D rendered images of the polyHIPEs from micro-CT, scale = 500µm.

2.6 Cell seeding

Scaffolds were cut into 7 mm in diameter and 2 mm in height using a cork borer No. 3, and any external layer was removed before with a scalpel. Due to the inherent hydrophobicity of the monomers used, the polyHIPEs surface was cleaned and activated with air plasma (0.8 mbar with a power of 50W for 60 s) and stored in PBS until used. PolyHIPEs were later sterilised by submerging them in 70% ethanol for 3 h under agitation, followed by three PBS washes. From each group, sterile polyHIPEs (n = 45) were assigned using an online random number generator (RNG) in groups of nine across five 24-well plates. The scaffolds were then immersed in cell culture media for 1 h. Afterwards, Y201 BMSCs cells, passage 79, were seeded dropwise onto scaffolds at a seeding density of $6x10^4$ cells in 50 µl of basal medium. Samples were placed in a humidified incubator at 37 ºC, 5% CO_2, for cell attachment. After 1 h, 450 µL of basal medium was added to each well, and after 24 h, scaffolds were transferred to a new plate. Each plate was assigned by RNG to be cultured for 7, 14, or 21 days in basal media

or for 21 days in osteogenic media. For scaffolds allocated to osteogenic conditions (two plates, n = 18), osteogenic supplements were added on day 3, consisting of 100 nM dexamethasone (D1756, Sigma), 50 µg mL^{-1} L-ascorbic acid 2-phosphate sesquimagnesium salt hydrate (A8960, Sigma), and 5 mM β-glycerophosphate disodium salt hydrate (G9422, Sigma). All cells were cultured in a humidified incubator at 37 ºC with 5% CO_2, and media was replenished every 7 days. Positive controls were cells grown on TCP (7600 cells per well) (25). Acellular scaffolds were used as negative controls and blanks, helping to account for any background signal from the scaffold material itself. Controls were cultured under the same conditions as the samples. Before experiments, resazurin, DNA quantification, ALP, SR (sirius red or direct red), AR (alizarin red), and fluorescence staining assays were pre-undertaken on Y201 BMSCs cultured on tissue culture polystyrene (TCP) to validate the assays. ALP was measured up to day 21, as prior research indicated that its levels in Y201 cells are either low or undetectable before this time (25,26).

Table 1. Median of pore diameter (Dp), and interconnects diameter (Dpt), mean ±SD of interconnects per pore (Nt), degree of Openness (DOO), density (ρ), % porosity (P) of polyHIPEs measured from SEM. Euler # obtained from micro-CT.

Internal phase (% v/v)	D_p (µm)	D_{pt} (µm)	N_t	DOO	ρ (g/cm^{-3})	P (%)	Euler #
75	70.4	4.84	6±4	0.031± 0.01	0.18 ± 0.03	72.8 ± 2.4	-600389
80	76.1	6.95	10±8	0.086± 0.06	0.13 ± 0.01	80.5 ± 3.8	-18462291
85	76.3	6.92	20 ±14	0.129± 0.06	0.11 ± 0.01	84.0 ± 4.2	-24287626

2.7 Resazurin reduction assay

The cell metabolic activity of Y201 BMSCs on the scaffolds was measured with a resazurin assay. Although resazurin is considered non-toxic, previous observations showed it can cause cell detachment after repeated assays over time (27). Therefore, assays were carried out in different scaffolds at 20 h (n = 3, per group), 7, 14, or 21 days of culture (n = 9 per group). Briefly, a 1 mM stock solution of resazurin sodium salt (R7017, Sigma) was prepared, filtered (0.2µm pore diameter, Fisher), and stored at 4 °C until used. A resazurin working solution (10% v/v) was prepared in PBS on the same day of use (27). After removing the media from the samples, 500 µL of the resazurin working solution was added to each sample and incubated in the dark for 2 h in a humidified incubator at 37 °C and 5% CO_2. Afterwards, 150 µL from each sample was transferred per triplicate into a 96-well plate and read using a microplate reader (Tecan infinite 200-pro), using an excitation wavelength of 540 nm and an emission wavelength of 590 nm. Immediately following resazurin measurement, scaffolds were rinsed three times with PBS and fixed with 3.7 % (w/v) formaldehyde (PFA) (252549, 35%, Sigma-Aldrich) for 40 min at RT. Scaffolds (n = 3 per group) were assigned using an online RNG for fluorescence staining, histological analysis, and confocal microscopy.

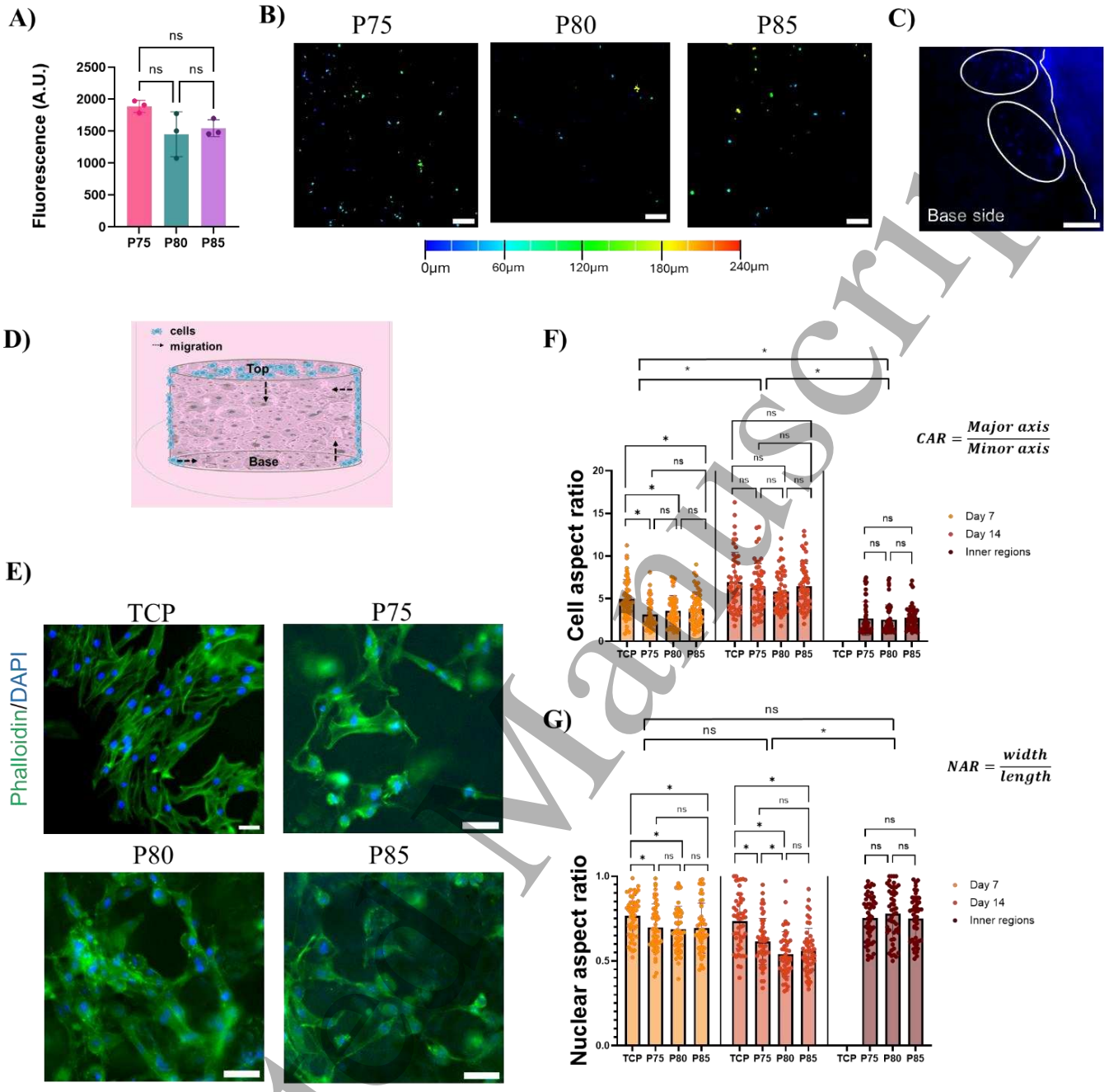

Figure 3. Cell seeding and differences of cell and nuclear morphology. A) Metabolic activity of Y201 BMSC cells on scaffolds assessed by resazurin reduction after cell seeding. One-way ANOVA and Tukey's multiple comparison ($\alpha = 0.05$) between groups, where ns = not significant. B) Confocal images of DAPI-stained cells on scaffolds after seeding. The colour scale indicates cell depth within scaffolds, scale bar =100 µm. C) Underside (base) of a scaffold after flipping, showing cells located near the scaffold's periphery, as indicated by the white line. Scale bar = 50 µm. D) Illustration of cell attachment to a scaffold after seeding, depicted as they were visualised in the microscope, showing potential cell migration across the scaffold's surface. E) Representative fluorescent images of Y201 cells cultured for 7 days. Cell nuclei were stained with DAPI (blue) and the actin cytoskeleton with Acti-stain 488 phalloidin (green), showing cell morphology on P75, P80, P85, and TCP scaffolds. Scale bar = 50 µm. F) Cell aspect ratio and G) nuclear aspect ratio of cells cultured on TCP or scaffolds for 7 and 14 days, as well as those in the inner regions (100 - 300 µm) of scaffolds after 21 days (n = 9 per group). One-way ANOVA followed by Tukey's multiple comparison test (7 and 14 days) or Kruskal-Wallis followed by Dunn's multiple comparison test (Inner regions), where $*P<0.05$, ns = not significant.

2.8 Fluorescence staining

PFA-fixed scaffolds (n = 3 per group) from day 7 were washed in PBS, permeabilized for 5 min with 0.1% v/v Triton X-100 (T8787, Sigma) made in PBS, blocked for 15 min with 1% w/v bovine serum albumin (A2153, LOT# SLBZ6632, Sigma) made in PBS, stained at RT in the dark for 40 min with 100 nM Acti-stain 488 Palloidin solution (PHDG1, LOT# 033, Cytoskeleton, Inc.) in PBS, and counterstained for 1 min with a 1:1000 of 10 mg mL^{-1} of 6-diamidino-2-phenylindole (DAPI, 32670, Sigma-Aldrich) solution in PBS. Scaffolds were rinsed with PBS, mounted on a microscope slide, and observed under a fluorescent microscope (Olympus, IX73) at 10X. Using ImageJ, cell and nuclear aspect ratios were measured in 50 cells from images of scaffolds. Cell aspect ratio (CAR) is defined as the major axis divided by the minor axis, while nuclear aspect ratio (NAR) is defined as width divided by length.

2.9 Histological analysis

PFA-fixed scaffolds (n = 3 per group) from day 21 were cut in half with a scalpel and placed in plastic histology cassettes (M493-Histosette). Sequential dehydration in Industrial Methylated Spirit (IMS) (99%, Fisher) (70%, 70% 80%, 85%, 90%, 95%, 100%, 100%), clarification in xylene (97%, Fisher), and paraffin wax infiltration was performed using a tissue processor (Leica, TP1020) for 18 h. Subsequently, each half of the scaffold was placed vertically in a wax box, dispensed with melted paraffin, and solidified on a cold plate (-10°C) in an embedding workstation (HistoStar, epredia). Sections of 5 µm were cut from the paraffin wax blocks with a microtome (Leica, RM2145). These were transferred to a paraffin section mounting bath (40 °C) to flatten them, mounted on a Superfrost adhesion microscope slide, and dried at 37 ºC for 48 h. Slides were deparaffinized with xylene twice for 5 min and transferred twice to 100% ethanol for 2 min. The slides were rehydrated with 90% IMS and dH_2O for 2 min each. The sections were stained with haematoxylin (105175, Merck) for 25 s, cleared in tap water, and rehydrated in 70% and 90% ethanol for 2 min each. The slides were then stained with eosin (117081, Merck) for 30 s and further dehydrated for 30 s in 100% ethanol. The slides were placed in xylene for 1 min and then for 5 min before mounting with DPX (D/5319, Thermo Fisher Scientific). Once DPX dried, pictures of the slides under a light microscope (Olympus CX43) at 4X were taken.

2.10 Confocal microscopy

PFA-fixed scaffolds (n = 3 per group) from day 21 were stained with 100 nM Acti-stain 488 Palloidin for 1.5 h at RT. Imaging was performed at 10X on a confocal microscope (Leica SP8 TCS) equipped with a 488 nm Argon laser. Confocal z-sections were made throughout the bottom and top of scaffolds using 4.2 µm steps, or approximately 97 steps, with an image format of 512 x 512. Around 97-93 images were stacked together to render a 3D image using the tools of LASX software.

2.11 DNA quantification and ALP measurement

After 21 days of cell culture with osteogenic supplements, scaffolds (n = 9 per group) were washed twice with PBS and then lysate overnight at -80 °C in a 10% v/v lysis buffer; 1M tris-solution (SC-296649, Chem Cruz), 1mM $ZnCl_2$ (208086, Sigma), 1mM $MgCl_2$ (M8266, Sigma) prepared with dH_2O with 1% v/v Triton-X100 (28). Subsequently, scaffolds were exposed to three freeze-thaw cycles (-80 ºC to 37 ºC), vortexed, and centrifuged for 5 min at 10 000 rpm. A 1:200 working solution was prepared by diluting the Quant-iT reagent in a Quant-iT buffer from a Quant-iT® dsDNA assay kit (Q33120, Invitrogen). Then, 10 µL of the cell lysate in triplicate and 90 µL of the working solution were added into a black 96-well plate, shaken in for 10 sec in a microplate reader, and incubated for 10 min to allow the DNA to conjugate with the reagent. Fluorescence was measured at an excitation wavelength of 485 nm and an emission wavelength of 535 nm. Samples were processed in three batches, and measured fluorescence was converted to ng of DNA using individual standard curves made with DNA standards. Following DNA quantification, ALP activity from the same samples was measured. ALP substrate solution was prepared by dissolving in 5 mL of 20% v/v diethanolamine buffer (34066, 5X, Thermo Fisher Scientific) diluted in dH_2O a tablet of p-nitrophenol phosphate (34047, Thermo Fisher Scientific). 10 µL of the cell lysate in triplicate and 90 µL of the ALP substrate solution were mixed in a 96-well plate. The plate was left at RT for around 15 min or until a yellowish colour appeared. Absorbance at 405 nm was read every min for 30 min with a microplate reader

(Tecan Infinite 200-Pro). ALP activity was indicated as nmol p-nitrophenol min^{-1} (nmolPNP min^{-1}), where one absorbance value is 19.75 nmol of product, then normalised to total DNA (29).

2.12 Alizarin red and direct red staining

Scaffolds (n = 9 per group) from cell culture in osteogenic supplements were fixed in 3.7 % (w/v) PFA for 40 min at RT, rinsed with dH_2O, and submerged in 1% w/v AR (pH = 4.1) (A5533, Sigma-Aldrich) for 30 min on an orbital shaker (150rpm) at RT. AR excess was removed by washing with dH_2O under orbital agitation. Then, 500 µL of 5% perchloric acid (311413, 60%, Sigma) was added for 15 min to destain the samples. 150 µL from each sample was transferred in triplicate to a 96-well plate and read in a microplate reader at 405 nm (29). After destaining, scaffolds were washed five times every 30 min with dH_2O.

1% w/v of Direct Red 80 (365548, 25%, Sigma) was prepared with picric acid (P6744, 1.3%, Sigma) and filtered (0.2 µm pore diameter, Fisher Scientific). For AR destaining, scaffolds were submerged in the solution for 18 h under orbital shaking (150 rpm), and the excess was removed by washing with dH_2O every 5 min. Scaffolds were de-stained for 20 min with a solution of 0.2 M NaOH:methanol (1:1) (30). 150 µL from each sample was transferred in triplicate to a 96-well plate and read using a microplate reader at an absorbance of 540 nm.

2.13 Statistical analysis

Results from polyHIPEs characterisation and FITC-dextran were averaged and presented as mean ± standard deviation (SD). Subsamples (triplicates) of each sample were averaged and taken as one reading. Blank data was also subtracted from each reading. Descriptive and statistical analyses were performed using GraphPad Prism 10 software (UK). Outliers were identified using the ROUT method (Q = 1). Outliers were removed from pore/diameter results before plotting the histograms. No data points were excluded for resazurin, ALP/DNA, AR, SR, nuclear aspect ratio, and cellular aspect ratio analyses. A normality test ($\alpha = 0.05$) was performed on the data (D'Agostino-Pearson). For data with a normal distribution, the differences between groups were determined by one-way or two-way analysis of variance (ANOVA), with a 95% confidence interval ($\alpha = 0.05$). Comparisons between groups were performed based on Tukey's multiple comparisons. Otherwise, the data was compared with a Kruskal-Wallis test and Dunn's multiple comparisons.

3. Results and discussion

3.1 Increased internal phase fraction on PolyHIPE structure

SEM observations of polyHIPEs' cross-sections showed spherical porous interconnected structures (Figure 2A). The porosity of the polyHIPEs correlated with their internal phase fraction (Table 1). Key structural parameters, including pore diameter, DOO, and the frequency and size of pore interconnects, were measured to characterise their porous structure further. The pore size ranged from 20 to 200 µm (Figure 2B), with median values of 70.4, 76.1, and 76.3 µm for P75, P80, and P85, respectively. Increasing the internal phase fraction from 75 to 85% v/v did not significantly affect the pore diameters. Since our study investigated the effect of scaffold interconnectivity in BMSCs behaviour, maintaining the pore size range across the polyHIPEs was fundamental. SEM images confirmed that pore interconnects were well-defined and spherical (Figure 2A), implying they formed during the emulsification process rather than post-washing steps (9). The size and frequency of interconnects per pore, along with the DOO, increased with the internal phase volume (Table 1). These findings align with previous observations observed with mercury intrusion porosimeter, which similarly showed an increase in both the number and diameter of pore interconnects with increasing internal phase (10). This effect arose because, while the number of particles used was sufficient to stabilise 75H, a slight increase in the internal phase volume created instabilities that enhanced interconnectivity within the polyHIPEs. This trend is consistent with findings from Owen et al., reporting a steady rise in DOO as the internal phase volume increased from 75 to 85% v/v (31). Similarly, Mert et al. noted that the internal phase fraction is a dominant factor in determining interconnect pore sizes, with larger sizes as the internal phase volume increases (32). This aspect of pore morphology is particularly relevant when considering the Euler number, a valuable topological descriptor for characterising the connectivity of porous structures. A lower Euler number signifies a greater number of holes and interconnections within the pore network, thus indicating enhanced pore

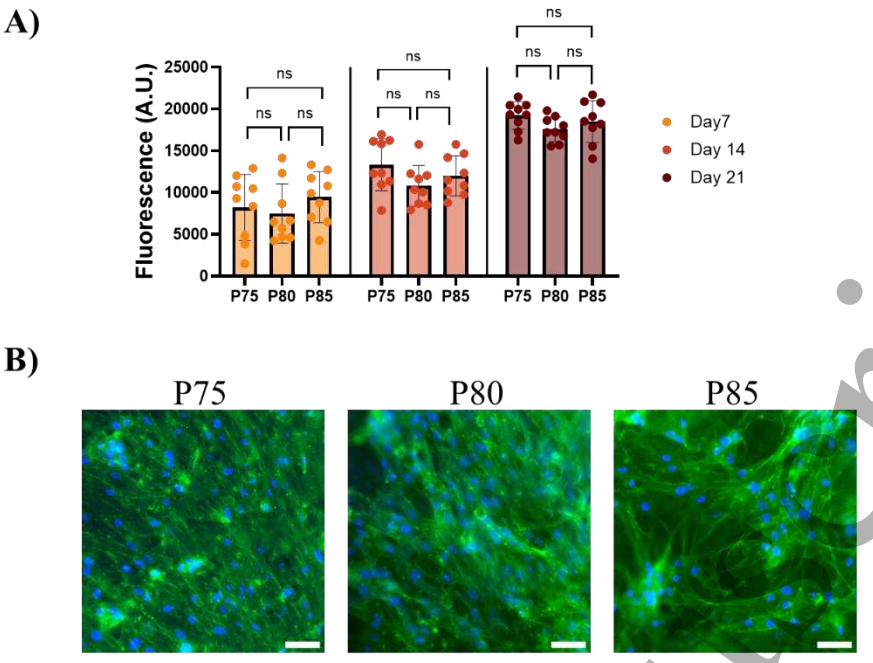

Figure 4. Proliferation of Y201 BMSC on scaffolds. A) Cell metabolic activity of Y201 BMSCs on P75, P80, and P85 after 7, 14, and 21 days of culture. Data are shown as mean ± SD (n = 9). Two-way ANOVA and Tukey's multiple comparison (α = 0.05) between groups at days 7, 14, and 21 showed scaffold type has no effect overall (ns). B) Y201 BMSCs after 21 days in culture in scaffolds, stained with DAPI and Acti-stain 488 phalloidin solution. Scale bar = 50µm.

connectivity (33). The Euler number (E) is calculated using the following relationship, where $\beta_o$is the number of pores, β_1 is the number of connections in the pore space, and β_2 is the number of closed cavities/pores (11).

$$E = \beta_o - \beta_1 + \beta_2 \quad (4)$$

3D micro-CT analysis revealed an inverse relationship between the Euler number and the DOO of the polyHIPEs (Table 1). This observation aligns with existing knowledge that the Euler number is influenced by porosity, pore diameter and pore geometry (33). These findings collectively demonstrate that size and number of pore interconnects/throats significantly impact the overall pore interconnectivity.

3.2 Attachment and proliferation was similar across the polyHIPEs

Y201 cell attachment was found to be similar on the three scaffolds, as determine by a resazurin assay (n=3 per group) (Figure 3A). Cells were observed to be distributed across the scaffold surfaces (Figure 3B). The maximum cell infiltration depth cells recorded from confocal images (n = 3 per group) were 103 ± 22 µm for P75, 138 ± 19µm for P80 and 189 ± 45µm for P85. The increased porosity and interconnectivity in P85 likely facilitated the deeper infiltration of cells into the scaffold structure. It is well-established that structural properties of scaffolds significantly influence cell seeding efficiency, often leading to cell trapping and aggregation on the scaffold's surface (34) or low attachment due to large pores, or sedimentation at the scaffold base due to cells falling through large interconnects (35) . Therefore, the cell distribution of the scaffolds after seeding can be directly attributed to variation in pore characteristics. Static seeding can sometimes lead to cell sedimentation at the bottom of scaffolds, but no cells were detected at the scaffold base. However, a significant number of cells adhered to some regions of the scaffolds' periphery, extending to the base side (Figure 3C). This peripheral attachment subsequently accounts for the presence of some cells on the bottom of the scaffolds (Figure 7). It is hypothesized that these cells migrated from the periphery to the scaffolds bottom surface over time, and then towards innermost part of the scaffolds, as documented before (35) (Figure 3D).

Y021 cells attached and oriented around the pores, preferably the large ones (Figure 3E). Cells positioned at the pore's struts, where they migrated in multiple directions along or towards more struts to form a "bridge" morphology, as shown in other studies (36). Cell morphology was assessed using the cell and nuclear aspect ratio and compared to cells cultured on a flat

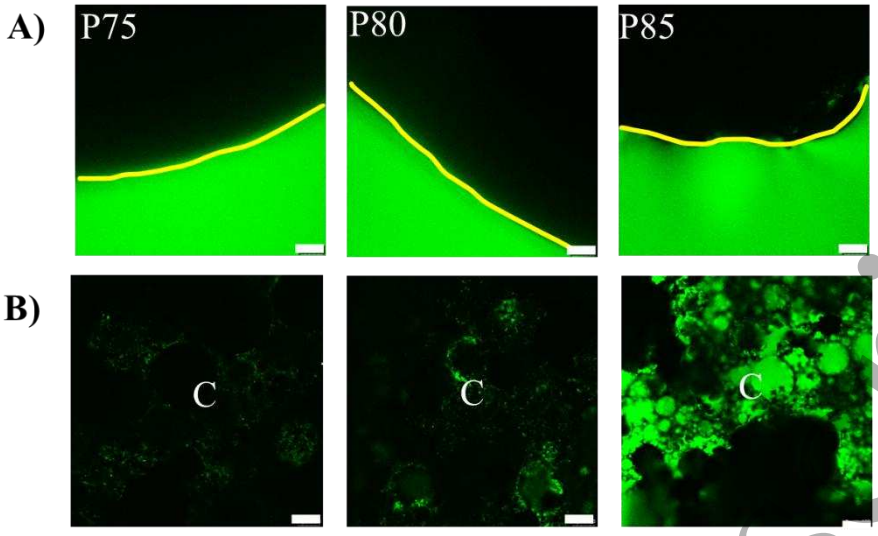

Figure 5. Lateral diffusion of FITC-dextran in polyHIPEs. Confocal microscopy images of FITC-dextran diffusion in polyHIPEs A) (t = 0 min) and B) (t = 15 min) showing the centre (C) of polyHIPEs, 2 mm from the periphery. The yellow lines show the periphery of each scaffold. The scale bar is 100 μm.

substrate, TCP. At day 7, Y201 BMSCs on TCP exhibited a more spread morphology with a median cell aspect ratio of 4.53. In comparison, cells seeded on scaffolds showed higher values, 2.66, 3.35, and 3.57 for P75, P80, and P85, respectively, with no significant differences between the scaffold groups (Figure 3F). This initial difference is likely due to the scaffolds' curved surface, which causes cells to adopt their shape to the curvature (37). As cells proliferate and spread to cover more of the surface, they become more elongated (6.3 for TCP, 6.2 for P75, 5.3 for P80 and 6.0 for P85). By day 14, the cell morphology on the scaffolds has become more like that on the TCP surface. The high aspect ratio observed in these cells is associated with cellular migration and spreading as they interact with the surface of scaffold and neighbouring cells (38).

At day 7, the nuclear aspect ratio, where values close to 1 indicate a more spherical structure and <1 a more elongated shape, medians were slightly lower for scaffolds, with values of 0.68, 0.66, and 0.67 for P75, P80, and P85, respectively, compared to 0.79 for TCP (Figure 3G). The slightly lower values on scaffolds were likely due to confined spaces. Cell migration through constricted spaces, such as pores, is limited by the nucleus, also noted in other studies involving MSC migration in constrained spaces (39,40). By day 14, this nuclear compression was more pronounced in scaffolds. Interestingly, cells found in inner regions of the scaffolds exhibited a reduction in the cellular aspect ratio and in consequence a less compress nucleus, as cells are moving to new areas, they adapt their shapes to the available surface area (37). While the nucleus can often recover from wrinkles made after passing through tight constrictions (41), further research is required to determine whether this process leads to DNA damage in our specific study.

In general, the porous architecture of scaffolds supports cell adhesion and proliferation. Actin fibres and nuclei staining after 21 days in culture confirmed that cells proliferated, extending across pores and eventually closing them (Figure 4B). However, no significant differences between the scaffolds by days of culture (Figure 4A) were observed by the resazurin reduction assay.

3.3 Pore interconnectivity enhanced dextran diffusion and Y201 BMSCs migration on the polyHIPEs

In this study, nutrient transport within the scaffolds occurred solely via diffusion due to static cell culture conditions. To assess diffusion within scaffolds, they were immersed in a FITC-dextran solution. To eliminate autofluorescence from scaffolds or petri dish, scaffolds were previous stained with Sudan black (Figure 5A). Confocal images were taken after 15 min. The diffusivity was inferred from the fluorescence intensity measured at the centre of the polyHIPEs. P85 exhibited the highest dextran diffusion, as demonstrated by significantly elevated fluorescence intensity compared to P75 and P80 (Figure 5B). Specifically, the relative

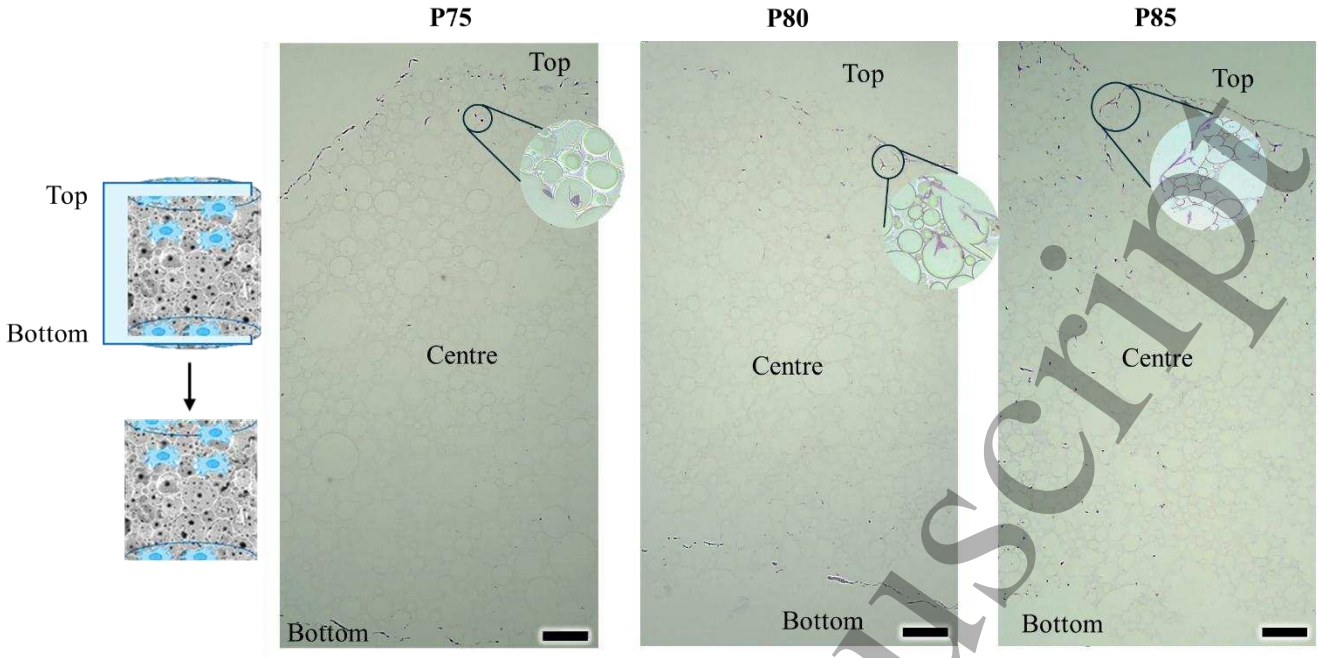

Figure 6. Cell migration observed in histological images. H&E staining of Y201 BMSCs on P75, P80, and P85 polyHIPEs over 21 days on culture. Scale bar = 100 µm. Zoom of cells (5X) show cell organisation through the scaffold.

fluorescence intensities were 5.9 ± 2.2, 8.1 ± 3.6, and 27 ± 4.2 for P75, P80, and P85, respectively. The increased diffusion observed in P85 can be attributed to enhanced porosity and interconnectivity, as the pore diameter range was maintained constant across the scaffolds. The diffusion of FITC-dextran was measured under static conditions, aligning with the experimental setup. While not assessed in this study, FITC-dextran flow could also be measured dynamically, for instance, by incorporating scaffolds into microfluidic devices (42). This would enable observation of the relationship between interconnectivity and permeability.

The migration of Y201 BMSCs into the scaffolds was observed by haematoxylin & eosin staining and confocal imaging after 21 days of culture. Staining (Figure 6) depicted that Y201 BMSCs initially lined the outer surface of the scaffolds, forming a dense cell layer. Over time, cells migrated from the scaffold's edges (top and bottom) towards the centre. Visually, among the scaffolds, P85 showed the most extensive cell infiltration, with more cells distributed throughout the scaffold cross-section. Confocal images further validated these findings, illustrating cell density and migration (Figure 7). Cell migration was defined as the depth at which the cells in the scaffolds were found, considering the first cells found on the scaffold surface. The migration depths from the top of the scaffold were 268 ± 81 µm for P75, 280 ± 52 µm for P80, and 348 ± 27 µm for P85. From the bottom of the scaffold, the corresponding migration depths were 245 ± 35 µm, 219 ± 50 µm, and 340 ± 31 µm, respectively. The P85 scaffolds exhibited the greatest migration depth, while P75 and P80 were comparable. Notably, this migration trend correlated with FITC-dextran diffusion results. Overall, studies emphasise the role of pore interconnectivity in scaffolds for efficient cell infiltration. Larger pore interconnects are associated with improved cell migration (43) and permeability. For example, Jia et al. (35) demonstrated that increased pore interconnect size enhanced cell movement and scaffold permeability. Similarly, Zhang et al. reported that a interconnected channels promotes greater cell migration in ceramic scaffolds (44). Together, these data indicate that a high pore interconnectivity was essential for promoting nutrient transport and BMSCs migration.

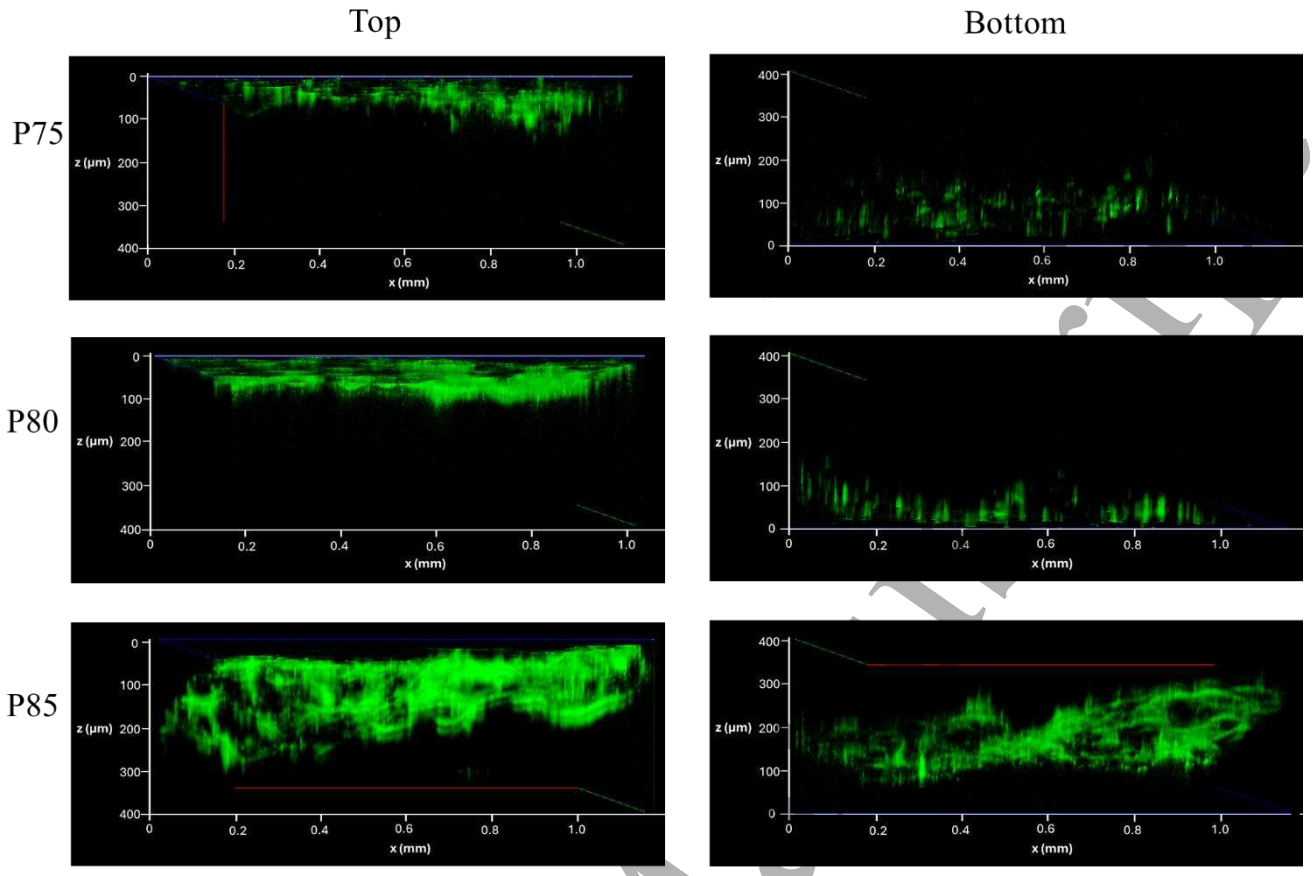

Figure 7. Cell migration observed with confocal microscopy. Lateral intensity projections of Y201 cells stained with Acti-stain 488 phalloidin within P75, P80, and P85 polyHIPEs after 21 days in culture.

3.4 PolyHIPE interconnectivity promoted the osteogenic differentiation of Y201 BMSCs

The early osteogenic differentiation of Y201 BMSCs was evaluated after 21 days of culture by assessing ALP activity and calcium and collagen deposition. ALP activity normalised to DNA content (Figure 8A) revealed that P85 had the highest ALP activity compared to P75 and P80. Specifically, the mean values were 0.59 ± 0.16 for P75, 0.60 ± 0.16 for P80, 1.39 ± 0.6 for P85, and 0.35 ± 0.11 nmol PNP min^{-1} ng^{-1} DNA for TCP. Additionally, extracellular calcium secretion and collagen production mirrored the ALP results, with P85 showing the highest calcium and collagen production. Quantitative results showed collagen production on P85 was approximately 1.8 times higher than for P75 or P80 (Figure 8C). Similarly, calcium deposition and ALP activity in P85 were 1.9 and 2.35 times higher than in P75 and P80 (Figure 8B).

Numerous studies emphasise the role of porous scaffold structures in enhancing the osteogenic differentiation of MSCs. For instance, Phadke et al. (45) and Fu et al. (46) compared scaffolds with two architectures, one porous and one more columnar, finding that a more porous scaffold led to greater MSC osteogenic differentiation. About the pore size, studies have shown that porous scaffolds with pores sizes larger than 400 um (47), around 300-100 µm (48) promoted the osteogenic differentiation of human MSCs. However, pore interconnectivity contributes to cell infiltration, promoting a 3D cell distribution that supports cell-cell and cell-matrix interactions relevant to osteogenic signalling and differentiation pathways (49,50). Studies have shown that such spreading and uniform distribution of cells within scaffolds increases osteogenic differentiation (51,52). Lo et al. further demonstrated that pore geometry and spatial constraints within scaffolds affect cytoskeleton organisation, impacting MSC differentiation (53). Therefore, the observed increase in osteogenic differentiation on P85 scaffolds can be attributed to its higher pore interconnectivity, facilitating cell ingrowth, homogeneous distribution,

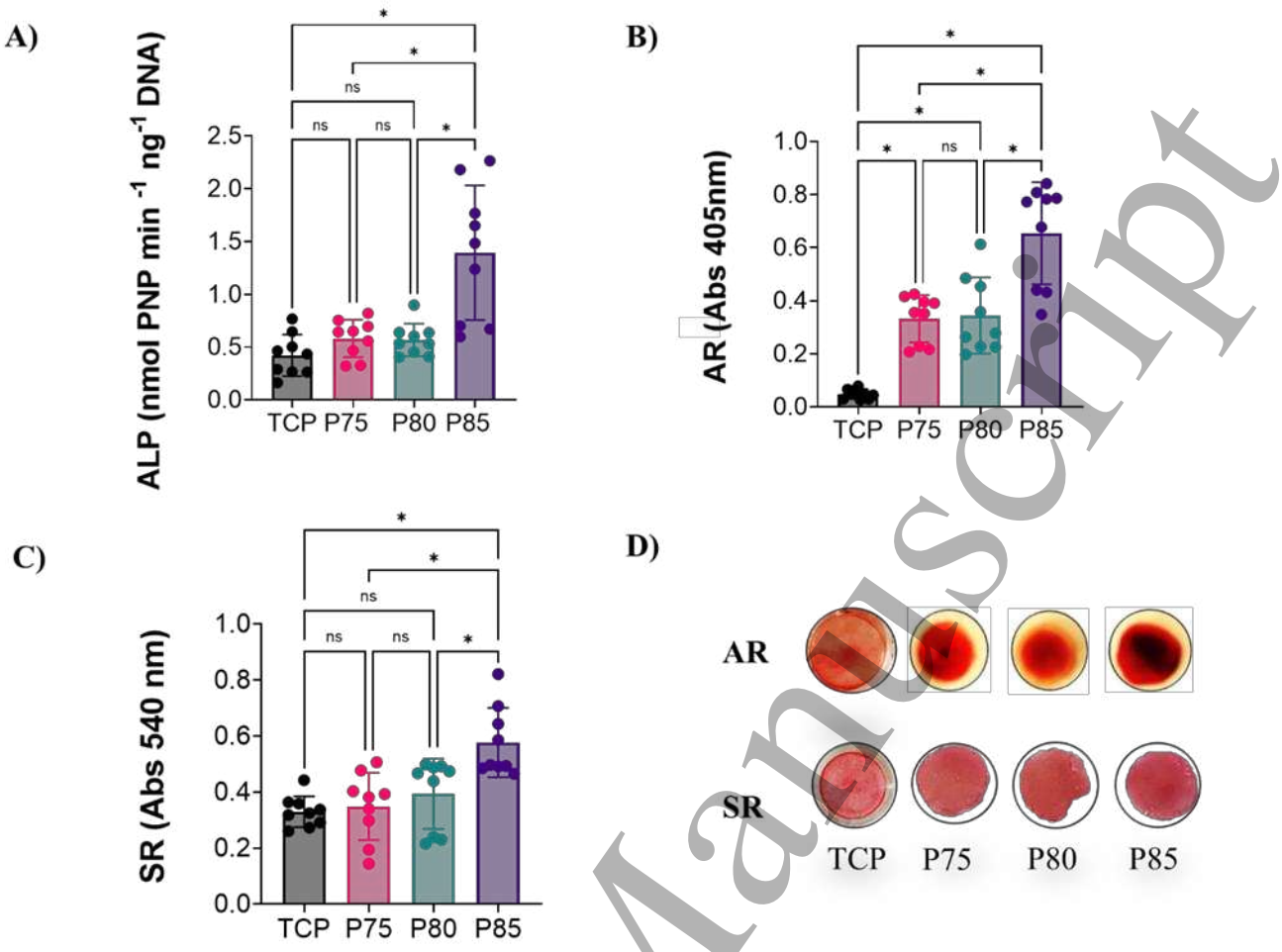

Figure 8. Osteogenic differentiation of Y201 BMSCs in scaffolds. A) ALP activity, B) AR, and C) SR quantification of Y201 BMSCs cultured on P75, P80, P85, or TCP in osteogenic differentiation medium for 21 days. Data are shown as mean ± SD (n = 9 per group). One-way ANOVA ($\alpha = 0.05$) and Tukey's multiple comparison tests were used, where *P<0.05, ns = not significant. D) Photo of scaffolds (Ø 7 mm) and TCP (Ø 14 mm) after AR or SR staining.

and cell signalling necessary for effective osteogenic responses.

4. Conclusions

This study synthesised porous scaffolds with a consistent pore size range but varied interconnectivity, enhancing tunability of scaffold characteristics crucial for bone tissue engineering. By increasing the internal phase fraction from 75% to 85%, the scaffolds exhibited a greater DOO along with a higher number and size of pore interconnects per pore, resulting in more effective nutrient diffusion, as observed through FITC-dextran diffusion tests under static conditions. Human BMSCs seeded onto these polyHIPEs demonstrated successful attachment and continuous proliferation over time. The results emphasise that higher pore interconnectivity promotes better cell infiltration and facilitates cell-cell and cell-extracellular matrix interactions, which could enhance osteogenic differentiation. Therefore, optimising pore interconnectivity is an important factor in scaffold design for BTE, as it directly influences cell behaviour and supports effective bone regeneration. Our novel method allows selectively tune this critical property. While this study investigated the effect of pore interconnectivity on MSC migration and infiltration, future research could explore the use of dynamic cell dynamic cell seeding and cell culture. This would provide valuable insights into cell distribution and migration under flow conditions.

Acknowledgements

AM-O acknowledges the scholarships granted by National Council of Science, Humanities and Technology (CONAHCYT). Authors thank Professor Paul Genever (University of York) for supplying the BMSC clonal line Y201.

Ethical statement

Ethical approval was not required for this work because the Y201 human bone marrow stromal cell line was provided by Professor Paul Genever of the University of York under a Material Transfer Agreement. The cell line's original derivation received ethical approval from the National Research Ethics Service and the University of Manchester, as previously documented (doi: 10.1038/s41598-018-27346-9).

References

1. Zhang Y, Wu D, Zhao X, Pakvasa M, Tucker AB, Luo H, et al. Stem Cell-Friendly Scaffold Biomaterials: Applications for Bone Tissue Engineering and Regenerative Medicine. Front Bioeng Biotechnol. 2020 Dec 14;8:598607.

2. Mukasheva F, Adilova L, Dyussenbinov A, Yernaimanova B, Abilev M, Akilbekova D. Optimizing scaffold pore size for tissue engineering: insights across various tissue types. Front Bioeng Biotechnol. 2024 Nov 12;12:1444986.

3. Abbasi N, Hamlet S, Love RM, Nguyen NT. Porous scaffolds for bone regeneration. Journal of Science: Advanced Materials and Devices. 2020 Mar;5(1):1–9.

4. Salehabadi M, Mirzadeh H. 3D Printing of Polyester Scaffolds for Bone Tissue Engineering: Advancements and Challenges. Adv Materials Technologies. 2025 Apr;10(8):2401522.

5. Gavazzo P, Viti F, Donnelly H, Oliva MAG, Salmeron-Sanchez M, Dalby MJ, et al. Biophysical phenotyping of mesenchymal stem cells along the osteogenic differentiation pathway. Cell Biol Toxicol. 2021 Dec;37(6):915–33.

6. Jiao J, Hong Q, Zhang D, Wang M, Tang H, Yang J, et al. Influence of porosity on osteogenesis, bone growth and osteointegration in trabecular tantalum scaffolds fabricated by additive manufacturing. Front Bioeng Biotechnol. 2023 Jan 27;11:1117954.

7. Deng F, Liu L, Li Z, Liu J. 3D printed Ti6Al4V bone scaffolds with different pore structure effects on bone ingrowth. J Biol Eng. 2021 Dec;15(1):4.

8. Armatas GS. Determination of the effects of the pore size distribution and pore connectivity distribution on the pore tortuosity and diffusive transport in model porous networks. Chemical Engineering Science. 2006 July;61(14):4662–75.

9. Aldemir Dikici B, Claeyssens F. Basic Principles of Emulsion Templating and Its Use as an Emerging Manufacturing Method of Tissue Engineering Scaffolds. Front Bioeng Biotechnol. 2020 Aug 12;8:875.

10. Durgut E, Sherborne C, Aldemir Dikici B, Reilly GC, Claeyssens F. Preparation of Interconnected Pickering Polymerized High Internal Phase Emulsions by Arrested Coalescence. Langmuir. 2022 Sept 13;38(36):10953–62.

11. Thomas A, Agarwal AK, Kashyap YS, Kumar IP, Bera J. Quantifying pore characteristics in polymer glass–ceramics composite scaffolds using micro-tomography. Journal of Materials Research. 2024 Apr 28;39(8):1258–72.

12. Elakkiya K, Bargavi P, Balakumar S. 3D interconnected porous PMMA scaffold integrating with advanced nanostructured CaP-based biomaterials for rapid bone repair and regeneration. Journal of the Mechanical Behavior of Biomedical Materials. 2023 Nov;147:106106.

13. Schiavi A, Gaido F, Gabrieli R, Alidoost D, Schwentenwein M, Mohammadi M, et al. Permeability and tomography-based microstructural analysis of ultra-porous bioactive glass scaffolds. Materials Letters. 2025 Apr;384:138064.

14. Munive-Olarte A, Hidalgo-Moyle JJ, Velasquillo C, Juarez-Moreno K, Mota-Morales JD. Boosting cell proliferation in three-dimensional polyacrylates/nanohydroxyapatite scaffolds synthesized by deep eutectic solvent-based emulsion templating. Journal of Colloid and Interface Science. 2022 Feb;607:298–311.

15. Freeman F, Browe D, Nulty J, Von Euw S, Grayson W, Kelly D. Biofabrication of multiscale bone extracellular matrix scaffolds for bone tissue engineering. eCM. 2019 Oct 11;38:168–87.

16. Nga NK, Hoai TT, Anh NTN, Kim S, Kim S, Kim HD, et al. Solvent casting-salt leaching synthesis, characterization, and biocompatibility of three-dimensional porous chitosan/nano-hydroxyapatite scaffolds for bone tissue engineering. Macromol Res. 2025 May;33(5):667–82.

17. Nayaju T, Shrestha D, Kang K, Maharjan B, Park CH. Reconstructed three-dimensional structure of gas-

foamed polycaprolactone/cellulose nanofibrous scaffold for biomedical applications. International Journal of Biological Macromolecules. 2025 Jan;285:138253.

18. Katrilaka C, Karipidou N, Petrou N, Manglaris C, Katrilakas G, Tzavellas AN, et al. Freeze-Drying Process for the Fabrication of Collagen-Based Sponges as Medical Devices in Biomedical Engineering. Materials. 2023 June 16;16(12):4425.

19. Tan JLT, Shimabukuro M, Tsuchiya A, Wijekoon WMRLK, Kishida R, Kawashita M, et al. Influence of porogens on architecture and osteogenesis of porous carbonate apatite artificial bones. Ceramics International. 2025 June;51(15):19963–72.

20. Durgut E, Claeyssens F. Pickering polymerized high internal phase emulsions: Fundamentals to advanced applications. Advances in Colloid and Interface Science. 2025 Feb;336:103375.

21. Wang Z, Gao T, Cui L, Wang Y, Zhang P, Chen X. Improved cellular infiltration into 3D interconnected microchannel scaffolds formed by using melt-spun sacrificial microfibers. RSC Adv. 2016;6(3):2131–4.

22. Aldemir Dikici B, Dikici S, Reilly GC, MacNeil S, Claeyssens F. A Novel Bilayer Polycaprolactone Membrane for Guided Bone Regeneration: Combining Electrospinning and Emulsion Templating. Materials. 2019;12(16).

23. Offeddu GS, Mohee L, Cameron RE. Scale and structure dependent solute diffusivity within microporous tissue engineering scaffolds. Journal of Materials Science: Materials in Medicine. 2020 May 4;31(5):46.

24. James S, Fox J, Afsari F, Lee J, Clough S, Knight C, et al. Multiparameter Analysis of Human Bone Marrow Stromal Cells Identifies Distinct Immunomodulatory and Differentiation-Competent Subtypes. Stem Cell Reports. 2015 June 9;4(6):1004–15.

25. Oliveira Rodrigues JR. Development of Osteoinductive Coatings for Spinal Implants (Fusion Cages). The University of Sheffield; 2022.

26. Bellucci D, Scalzone A, Ferreira AM, Cannillo V, Gentile P. Adhesive Bioinspired Coating for Enhancing Glass-Ceramics Scaffolds Bioactivity. Materials. 2022 Nov 15;15(22):8080.

27. Hann AJ. Development and Assessment of In Vitro Models of Osteogenic Microstructures. The University of Sheffield; 2023.

28. Bhaskar B, Owen R, Bahmaee H, Rao PS, Reilly GC. Design and Assessment of a Dynamic Perfusion Bioreactor for Large Bone Tissue Engineering Scaffolds. Applied Biochemistry and Biotechnology. 2018 June 1;185(2):555–63.

29. Delaine-Smith RM, Hann AJ, Green NH, Reilly GC. Electrospun Fiber Alignment Guides Osteogenesis and Matrix Organization Differentially in Two Different Osteogenic Cell Types. Front Bioeng Biotechnol. 2021 Oct 25;9:672959.

30. Sittichokechaiwut A, Edwards J, Scutt A, Reilly G. Short bouts of mechanical loading are as effective as dexamethasone at inducing matrix production by human bone marrow mesenchymal stem cell. Eur Cell Mater. 2010 July;20:45–57.

31. Owen R, Sherborne C, Paterson T, Green NH, Reilly GC, Claeyssens F. Emulsion templated scaffolds with tunable mechanical properties for bone tissue engineering. Journal of the Mechanical Behavior of Biomedical Materials. 2016 Feb;54:159–72.

32. Mert HH, Mert MS, Mert EH. A statistical approach for tailoring the morphological and mechanical properties of polystyrene PolyHIPEs: looking through experimental design. Mater Res Express. 2019 Sept 25;6(11):115306.

33. Mason PE, Darvell LI, Jones JM, Williams A. Comparative Study of the Thermal Conductivity of Solid Biomass Fuels. Energy Fuels. 2016 Mar 17;30(3):2158–63.

34. Ali D. Effect of scaffold architecture on cell seeding efficiency: A discrete phase model CFD analysis. Computers in Biology and Medicine. 2019 June;109:62–9.

35. Jia G, Huang H, Niu J, Chen C, Weng J, Yu F, et al. Exploring the interconnectivity of biomimetic hierarchical porous Mg scaffolds for bone tissue engineering: Effects of pore size distribution on mechanical properties, degradation behavior and cell migration ability. Journal of Magnesium and Alloys. 2021 Nov;9(6):1954–66.

36. Buenzli PR, Lanaro M, Wong CS, McLaughlin MP, Allenby MC, Woodruff MA, et al. Cell proliferation and migration explain pore bridging dynamics in 3D printed scaffolds of different pore size. Acta Biomaterialia. 2020 Sept;114:285–95.

37. Werner M, Blanquer SBG, Haimi SP, Korus G, Dunlop JWC, Duda GN, et al. Surface Curvature Differentially Regulates Stem Cell Migration and Differentiation via

Altered Attachment Morphology and Nuclear Deformation. Advanced Science. 2017 Feb;4(2):1600347.

38. Banik BL, Riley TR, Platt CJ, Brown JL. Human Mesenchymal Stem Cell Morphology and Migration on Microtextured Titanium. Front Bioeng Biotechnol. 2016 May 10;4.

39. Doolin MT, Ornstein TS, Stroka KM. Nuclear Deformation in Response to Mechanical Confinement is Cell Type Dependent. Cells. 2019 May 8;8(5):427.

40. Lu Q, Diao J, Wang Y, Feng J, Zeng F, Yang Y, et al. 3D printed pore morphology mediates bone marrow stem cell behaviors via RhoA/ROCK2 signaling pathway for accelerating bone regeneration. Bioactive Materials. 2023 Aug;26:413–24.

41. McKee B, Abolghasemzade S, Wang TC, Harsh K, Kaur S, Blanchard R, et al. Excess surface area of the nuclear lamina enables unhindered cell migration through constrictions. Sci Adv. 2025 Mar 28;11(13).

42. Bahmaee H, Owen R, Boyle L, Perrault CM, Garcia-Granada AA, Reilly GC, et al. Design and Evaluation of an Osteogenesis-on-a-Chip Microfluidic Device Incorporating 3D Cell Culture. Front Bioeng Biotechnol. 2020 Sept 8;8:557111.

43. Singh YP, Dasgupta S, Agrawal AK, Bhaskar R. Quantitative analysis of reinforcement of nano-sized monetite particles on chitosan/gelatin 3D porous scaffolds using the micro-CT technique. J Porous Mater. 2025 May 7;

44. Lu JX, Flautre B, Anselme K, Hardouin P, Gallur A, Descamps M, et al. Role of interconnections in porous bioceramics on bone recolonization in vitro and in vivo. Journal of Materials Science: Materials in Medicine. 1999;10(2):111–20.

45. Phadke A, Hwang Y, Hee Kim S, Hyun Kim S, Yamaguchi T, Masuda K, et al. Effect of scaffold microarchitecture on osteogenic differentiation of human mesenchymal stem cells. eCM. 2013 Jan 18;25:114–29.

46. Fu Q, Rahaman MN, Bal BS, Brown RF. Proliferation and function of MC3T3-E1 cells on freeze-cast hydroxyapatite scaffolds with oriented pore architectures. J Mater Sci: Mater Med. 2009 May;20(5):1159–65.

47. Wang Y, Liu Y, Chen S, Francis Siu MF, Liu C, Bai J, et al. Enhancing bone regeneration through 3D printed biphasic calcium phosphate scaffolds featuring graded pore sizes. Bioactive Materials. 2025 Apr;46:21–36.

48. Brennan CM, Eichholz KF, Hoey DA. The effect of pore size within fibrous scaffolds fabricated using melt electrowriting on human bone marrow stem cell osteogenesis. Biomed Mater. 2019 Nov 8;14(6):065016.

49. Yun C, Kim SH, Kim KM, Yang MH, Byun MR, Kim JH, et al. Advantages of Using 3D Spheroid Culture Systems in Toxicological and Pharmacological Assessment for Osteogenesis Research. IJMS. 2024 Feb 21;25(5):2512.

50. Zauchner D, Müller MZ, Horrer M, Bissig L, Zhao F, Fisch P, et al. Synthetic biodegradable microporous hydrogels for in vitro 3D culture of functional human bone cell networks. Nat Commun. 2024 June 13;15(1):5027.

51. Melke J, Zhao F, Ito K, Hofmann S. Orbital seeding of mesenchymal stromal cells increases osteogenic differentiation and bone-like tissue formation. Journal Orthopaedic Research. 2020 June;38(6):1228–37.

52. Yang Y, Wang X, Wang Y, Hu X, Kawazoe N, Yang Y, et al. Influence of Cell Spreading Area on the Osteogenic Commitment and Phenotype Maintenance of Mesenchymal Stem Cells. Sci Rep. 2019 May 3;9(1):6891.

53. Lo YP, Liu YS, Rimando MG, Ho JHC, Lin K hui, Lee OK. Three-dimensional spherical spatial boundary conditions differentially regulate osteogenic differentiation of mesenchymal stromal cells. Sci Rep. 2016 Feb 17;6(1):21253.